Open Research Online

The Open University's repository of research publications
and other research outputs

Mid-ultraviolet Hubble Observations of Europa and the Global Surface Distribution of SO$_2$

Journal Item

oro.open.ac.uk

Mid-ultraviolet Hubble Observations of Europa and the Global Surface Distribution of SO₂

Tracy M. Becker[1,2] , Samantha K. Trumbo[3,4] , Philippa M. Molyneux[1] , Kurt D. Retherford[1,2] , Amanda R. Hendrix[5] ,
Lorenz Roth[6] , Ujjwal Raut[1,2] , Juan Alday[7,8] , and Melissa A. McGrath[9]

[1] Southwest Research Institute, San Antonio, TX, USA; tracy.becker@swri.org
[2] University of Texas at San Antonio, San Antonio, TX, USA
[3] Division of Geological and Planetary Sciences, California Institute of Technology, Pasadena, CA 91125, USA
[4] Center for Astrophysics and Planetary Science, Cornell University, Ithaca, NY 14853, USA
[5] Planetary Science Institute, Tucson, AZ, USA
[6] KTH Royal Institute of Technology, Stockholm, Sweden
[7] AOPP, Department of Physics, University of Oxford, UK
[8] School of Physical Sciences, The Open University, Milton Keynes, UK
[9] NASA Marshall Space Flight Center, Huntsville, AL, USA
Received 2021 August 5; revised 2022 April 19; accepted 2022 April 22; published 2022 June 2

Abstract

We present spatially resolved reflectance spectra of Europa's surface in the wavelength range of 210–315 nm obtained by the Hubble Space Telescope Imaging Spectrograph in 2018 and 2019. These data provide the first high-quality, near-global spectral observations of Europa from 210 to 240 nm. They show that the reflectance of Europa's leading, trailing, anti-Jovian, and sub-Jovian hemispheres is ∼5% near 210 nm, with varying spectral slopes across the mid-UV. This low albedo, even on the more "pristine" leading hemisphere, indicates a lack of the signature far-UV spectral edge characteristic of water ice. We detected and mapped a strong absorption feature at 280 nm that is consistent with an S–O bond that has previously been attributed to SO₂ on the surface, hypothesized to be formed through radiolytic processing of Iogenic sulfur ions that have been preferentially emplaced on Europa's trailing hemisphere by Jupiter's magnetic field. Our models show that small inclusions of SO₂ (0.1%) within the water ice are sufficient to produce the 280 nm feature without producing a feature at 4.07 μm, which has not been observed in ground-based spectral observations of Europa. This data set is the first to produce a spatially resolved, near-global map of the assumed SO₂ feature, which is primarily concentrated near the apex of the trailing hemisphere and correlated with large-scale darker regions in both the visible and the ultraviolet. This distribution is consistent with "cold" exogenic sulfur ion bombardment on Europa.

1. Introduction

Jupiter's moon Europa is characterized by its bright, icy shell that is primarily composed of water ice harboring a liquid water ocean below. It is the primary target of NASA's upcoming Europa Clipper mission and will be explored through several close encounters during the European Space Agency's upcoming JUICE mission.

While the primary constituent of Europa's relatively young surface is water ice, non-water-ice materials have also been detected across the surface and are often associated with albedo variations observed at visible wavelengths (e.g., Carlson et al. 2009). Determining whether these non-water-ice species are endogenic or exogenic in origin is important for understanding Europa's formation and subsequent evolution and assessing whether the surface material can provide insights into the composition of the subsurface ocean below.

Though limited, observations of Europa in the ultraviolet (UV) have revealed spectral features that have implications for its composition and the processes that occur on the moon's surface. Disk-integrated observations of Europa by the International Ultraviolet Explorer (IUE) revealed a spectral

absorption band centered near 280 nm (Lane et al. 1981). It was later demonstrated that the strength of the absorption band was correlated with longitude (Ockert et al. 1987; Domingue & Verbiscer 1997), diminishing in strength with increasing distance from the apex of Europa's trailing hemisphere (270° W longitude). Disk-integrated observations with a higher signal-to-noise ratio (S/N) collected by the Faint Object Spectrograph (FOS) instrument on the Hubble Space Telescope (HST) confirmed the presence of a strong absorption feature on Europa's trailing hemisphere (Noll et al. 1995).

The disk-resolved images of Europa in the UV that were collected by the Galileo Ultraviolet Spectrometer captured swaths of Europa's trailing and anti-Jovian hemispheres at wavelengths from 240 to 320 nm with spatial resolutions between 55 and 740 km (Hendrix et al. 1998). These observations substantiated previous observations that the trailing hemisphere has a lower UV albedo and that the 280 nm spectral feature generally appears to decrease in strength with distance from the trailing hemisphere apex. Analyses of the higher spatial resolution Galileo data further supported the large-scale pattern of the feature, with some indication of effects from local terrain (Hendrix et al. 2011).

The 280 nm feature has been attributed to the A–X transition in an S–O bond within surface SO₂ based on the limited laboratory data at these wavelengths and temperatures (Lane et al. 1981; Sack et al. 1992; Noll et al. 1995; Herzberg 1996;

Table 1
Geometry of HST Europa Observations

Hemisphere	Date (UTC) YYYY-MM-DD	Time Start (UTC) HH:MM:SS	Subobserver Longitude (deg)	Subobserver Latitude (deg)	Europa Angular Diameter (arcsec)	Pole Orientation (deg)	STIS Slit Orientation (deg E of N)	Phase Angle (deg)
Anti-Jovian	2018-04-11	07:09:29	196.4	−3.89	0.953	15.69	−101.90	5.35
Trailing	2018-04-19	02:42:25	268.03	−3.88	0.964	15.98	−151.60	3.95
Sub-Jovian	2018-06-01	10:03:00	342.75	−3.74	0.963	17.71	84.40	4.60
Leading	2019-06-21	07:23:21	89.3	−3.14	1.003	4.77	48.91	2.18

Note. The STIS slit orientation is the position angle of the image y-axis in degrees east of celestial north.

Hendrix et al. 1998). While SO_2 may not be the only material capable of producing the 280 nm feature, it is currently the only relevant compound that has been measured in the lab that is consistent with the observations. For example, olivines and magnetite have measurable absorption bands at 280 nm (Cloutis et al. 2008); however, both of those materials exhibit features near 225–230 nm that are not detected in our data set and a strong, broad absorption feature centered near 1 μm that does not appear to be consistent with the visible observations of Europa. Further, the distribution of the feature is also consistent with spectral signatures observed in the visible that were attributed to sulfur allotropes (Spencer et al. 1995; Trumbo et al. 2020). We therefore refer to this sulfur-based feature as SO_2 throughout this work. Its concentration on the trailing hemisphere has led to the hypothesis that the SO_2 is produced via radiolytic processing of exogenic sulfur ions originating from Io that were swept up by Jupiter's magnetosphere and preferentially deposited on Europa's trailing hemisphere (Lane et al. 1981; Hendrix et al. 2011). However, it is also possible that some fraction of the sulfur is endogenic to Europa and preferentially exposed to magnetospheric bombardment and erosion of the trailing hemisphere surface (Noll et al. 1995; Hendrix et al. 2011). More precise measurements of the shape and distribution of the SO_2 feature and how it compares with the overall UV darkening of the surface may help to distinguish between hypotheses pointing to an endogenic or exogenic origin.

We observed Europa using the HST Space Telescope Imaging Spectrograph (STIS) instrument to obtain the first near-global UV data between 180 and 320 nm at a high spatial resolution of ~80 km pixel^{-1} along the slit, though, due to S/N, we focus on the data between 210 and 315 nm. These observations were designed to explore Europa's surface in the mid-UV, including previously unobserved wavelengths, with high spatial resolution. Like previous observations, we detect a strong spectral feature centered near 280 nm that is strongest near the apex of the trailing hemisphere. In Section 2, we describe our observations and how the data were processed. We discuss how we analyzed the UV spectra in Section 3 and present the first global maps of the 280 nm feature in Section 4. In Section 5, we compare our observations with spectral models. Finally, we discuss the implications of our observations, analysis, and results in Section 6 and provide a summary conclusion in Section 7.

2. Observations and Data Processing

We observed Europa with HST/STIS using the near-UV Multi-Anode Microchannel Array (MAMA) detector in 2018 and 2019 on four separate visits consisting of one orbit each. The observations were taken in the first-order spectroscopy

mode with the G230L grating and the 52 arcsecond × 0.2 arcsecond slit, which is imaged onto the array detector.

The observations of the trailing, anti-Jovian, and sub-Jovian hemispheres were completed in 2018 April and June. Due to a gyro issue for HST in 2018 June, we were unable to acquire data on the leading hemisphere that year; these observations were obtained in 2019 June.

During each observation, we stepped the 0.2 arcsecond wide slit across Europa's surface twice. We offset the slit by −0.1 arcsecond from the subobserver point in the direction perpendicular to the slit for the first exposure, then offset the slit by +0.1 arcsecond along the same direction for the second exposure, covering a 0.4 arcsecond wide swath of Europa's surface. Details about the observing geometry are provided in Table 1. Each exposure time was 987 s, with the exception of the observations of the leading hemisphere, which used exposure times of 808 and 777 s for the first and second exposures, respectively.

Europa's angular diameter ranged from 0.953″ to 1.003″ over the four observations. For the observations of the trailing, sub-Jovian, and anti-Jovian hemispheres, reflected sunlight from Europa was captured in the centermost 38 STIS pixels, and for the leading hemisphere (when Europa was largest), signal was obtained across 41 STIS pixels. This corresponds to a spatial resolution of approximately 76–82 km pixel^{-1} along the slit.

The raw 2D spectra were reduced and calibrated to "x2d" files by the HST pipeline using the CALSTIS software. After binning the data over the spectral dimension, we fit a Gaussian to identify the pixels containing reflected sunlight from Europa. To determine the noise as a function of wavelength, we use two spatial regions above and below the region of maximum signal that span 100 pixels each and are located 10 times the FWHM of the Gaussian away from the peak signal. We sum the noise regions, remove that signal from each pixel containing reflected light from Europa, and propagate the errors.

To obtain reflectance from the observed flux, we use the solar flux data from the same dates as our observations collected by the Total and Spectral Solar Irradiance Sensor (TSIS-1) and the SORCE/SOLSTICE ultraviolet spectrograph, both archived on the LASP Interactive Solar Irradiance Datacenter (McClintock et al. 2005). We use the higher spectral resolution SORCE/SOLSTICE data to remove the solar signal for our analysis of the mid-UV (Section 3.1) and TSIS-1 data when analyzing the 280 nm feature (Section 3.2) because the solar spectrum extends slightly further into the near-UV and allows us to better assess the full shape of 280 nm feature. We reduce the high spectral resolution of the solar observations to match that of the STIS observations, which is 1.548 Å pixel^{-1}. Prior to dividing out the solar signal from
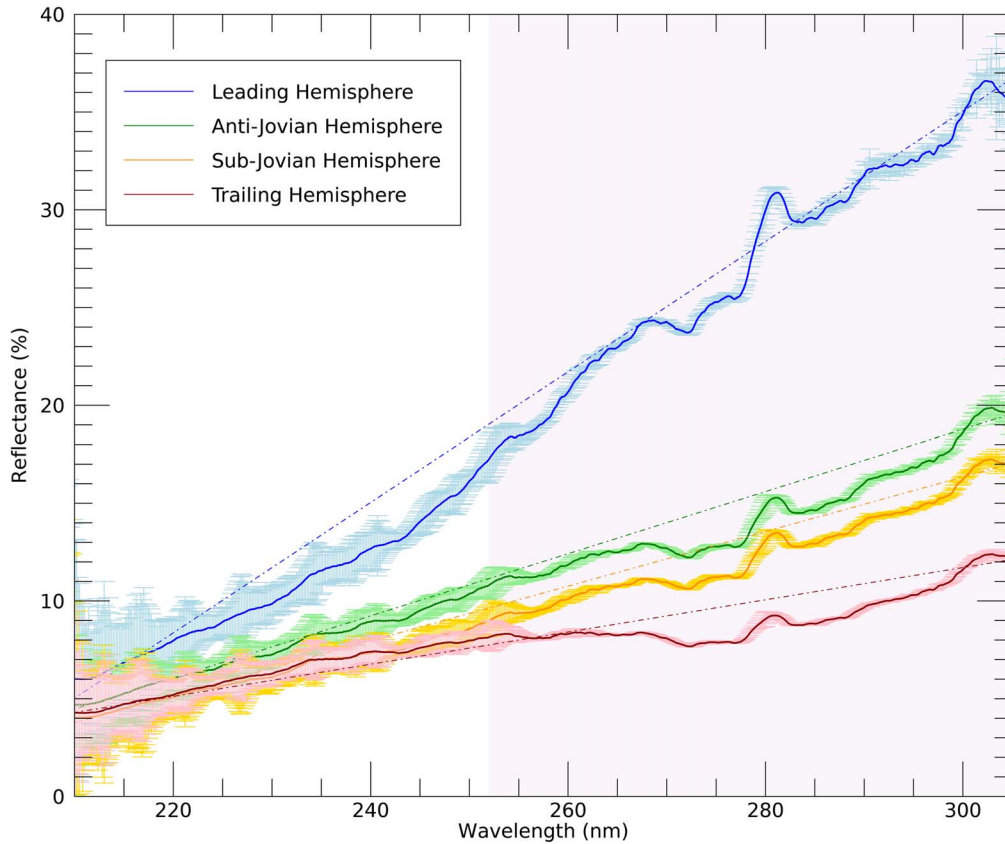
Figure 1. Mid-UV reflectance of Europa's leading, trailing, sub-Jovian, and anti-Jovian hemispheres. We bin the 10 centermost STIS spatial pixels and average the reflectance from the two slit positions on each hemisphere, producing one spectrum near the apex of each hemisphere. The spectra are also smoothed by 20 data points. We use the SORCE/SOLSTICE to remove the solar signal for the mid-UV assessment. The dashed line represents a linear fit to the data. The narrower bumps in the spectra, including those near 280 nm, are due to the incomplete removal of solar features. The broad 280 nm feature of interest for this work, which spans 253–305 nm, is indicated by the light purple region. The very broad 230 nm feature observed only in the leading hemisphere spectra extends from ∼200 to 260 nm.

Europa's reflected solar flux, we smooth the spectra with a boxcar average of 10 pixels to further improve the S/N. Following Feldman et al. (2000), we calculate the reflectance (R) as the ratio of the reflected flux to the solar flux at Europa,

$$R = \left(\frac{F_{E}(\lambda)}{F_{\odot}(\lambda)} \right) \frac{\pi d^2}{\Omega}, \qquad (1)$$

where d is the Sun–Europa distance (in au), Ω is the solid angle of the STIS pixels in steradians, $F_{\odot}$ is the solar flux at 1 au, and F_{E} is the flux from Europa. We propagate the errors reported for the TSIS-1, SORCE/SOLSTICE, and STIS data accordingly. This calculation determines the reflectance of Europa within each pixel rather than the albedo because we do not account for the phase function ϕ in this work, since here we primarily focus on the relative band strength of the features rather than brightness comparisons between hemispheres or planetary bodies.

3. Data Analysis

3.1. The Spectrum of Europa in the Mid-UV

The mid-UV spectra of Europa derived from the HST data are shown in Figure 1. For this analysis, we apply the data reduction described in Section 2 to the 10 central pixels for each of the two slit positions per hemisphere and then average those data to acquire one spectrum. We do not integrate over the entire HST slit, instead showing the results for the

reflectance near the central longitude, or apex, of each hemisphere. The apex is located at 0°, 90°, 180°, and 270° for the sub-Jovian, leading, anti-Jovian, and trailing hemispheres, respectively.

The mid-UV spectrum of Europa is red-sloped, and its steepness varies for each hemisphere; the leading hemisphere has the strongest red slope, while the trailing hemisphere's spectrum rises more gradually from the far UV into the mid-UV. The spectrum is very dark (reflectance ∼ 5%) for all Europa hemispheres at wavelengths <210 nm and gradually increases in brightness with increasing wavelength. The leading hemisphere displays a higher reflectance than the other hemispheres across the mid-UV, in a pattern similar to that observed at visible wavelengths and in previous mid-UV observations (e.g., Hendrix et al. 2005; Carlson et al. 2009).

Two spectral features are apparent in the data: (1) a broad, shallow 280 nm absorption feature most clearly observed in the trailing hemisphere data and (2) a broad, shallow absorption feature centered near 230 nm only observed near the leading hemisphere (Trumbo et al. 2022). The first feature is the subject of this paper and has been attributed to the A–X transition of an S–O bond, likely SO_2 on the surface, and was observed in data from the IUE, HST FOS, and Galileo-UVS (Lane et al. 1981; Sack et al. 1992; Noll et al. 1995; Herzberg 1996; Hendrix et al. 1998). In the following sections, we analyze the strength of this absorption feature, map its spatial distribution, and produce models to constrain the amount of SO_2 present to produce this spectral feature.
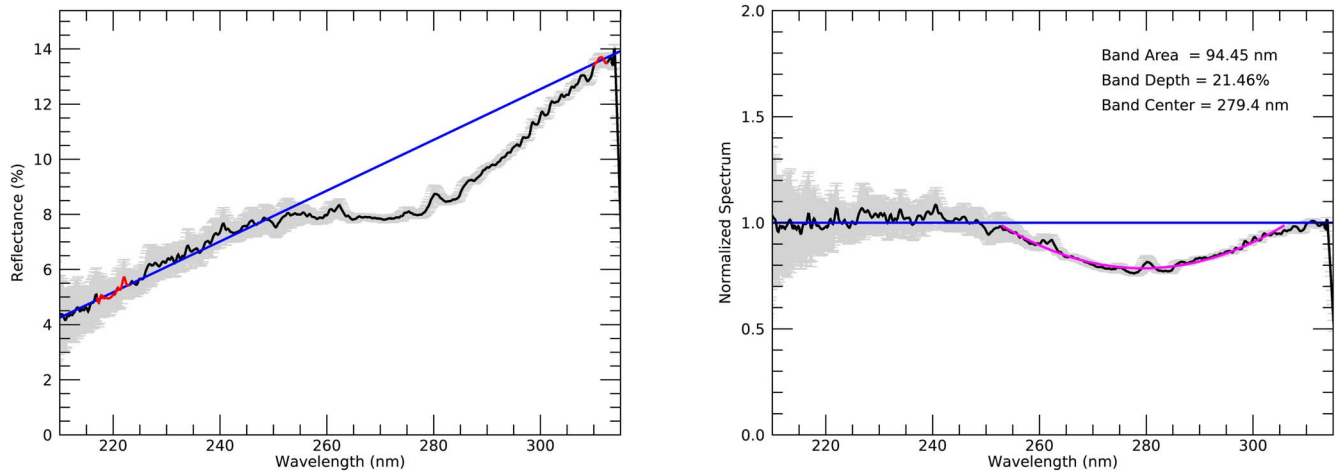
Figure 2. (Left) Linear fit (blue) to the spectral continuum of the trailing hemisphere of Europa. Regions used in the linear fit are marked in red. (Right) Trailing hemisphere spectrum with the continuum removed and a parabolic fit to the absorption feature centered at 279.4 nm.
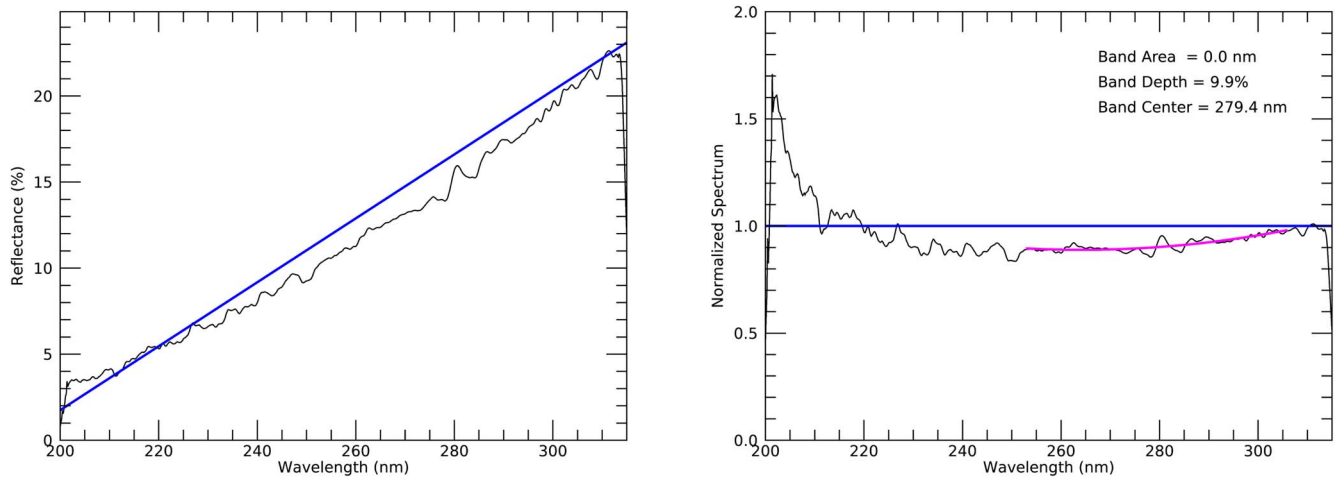

Figure 3. The central pixel from the sub-Jovian hemisphere shows an example of how the normalized spectrum appears when both the 280 and 230 nm features are present and overlapping. Pixels with this much overlap are flagged to indicate a likely overestimate of the band area of the 280 nm feature due to the additional absorption from the 230 nm feature. In these cases, we force the band depth measurement to occur at 279.4 nm to avoid being affected by the overlapping feature.

The second broad absorption feature is centered near 230 nm and has apparently not been previously reported in observations of Europa, since few other observations cover this spectral region. This feature is most clearly observed on the leading hemisphere and is not detectable on the trailing hemisphere. A detailed analysis of this feature and its distribution is described in Trumbo et al.'s (2022) detection paper; we include some details about its strength and distribution in Section 3.2.

3.2. SO₂ Feature

As described in Section 1, the 280 nm absorption feature has been attributed to SO_2 (Lane et al. 1981; Noll et al. 1995; Hendrix et al. 1998). Noll et al. (1995) found a strong match between trailing hemisphere HST/FOS observations of Europa with the laboratory experiments measuring the transmittance spectrum of SO_2 ice layers grown on H_2O ice performed by Sack et al. (1992). The laboratory database of materials in the UV is limited, but there are currently no other relevant materials known to match the spectral extent and position of the 280 nm absorption feature.

We perform a detailed analysis of the SO_2 absorption feature centered near 280 nm. Since the spectral feature appears strongest near the apex of the trailing hemisphere, we perform an initial assessment of its shape and strength at that location. We bin the centermost 10 spatial pixels (detector rows) on the trailing hemisphere from each of the two slit positions and average their spectra across the two observations. We remove the spectral continuum by fitting a line to the average signal between 217 and 223 nm and the average signal between 310 and 312.5 nm. After dividing by the continuum, we then fit a second-order polynomial (parabola) to the spectral feature to identify the band center (279.4 nm) at the minimum of the parabola and the approximate width of the feature, which spans 253.0–305.8 nm; see Figure 2. The width determined here is then used as the bounds for the spectral feature when analyzing each pixel individually. We determine the band area using two techniques: integrating the area under the parabolic curve between 253.0 and 305.8 nm and simply integrating the parabolic fit. These techniques result in very similar values. The band depth is calculated at the band center by simply
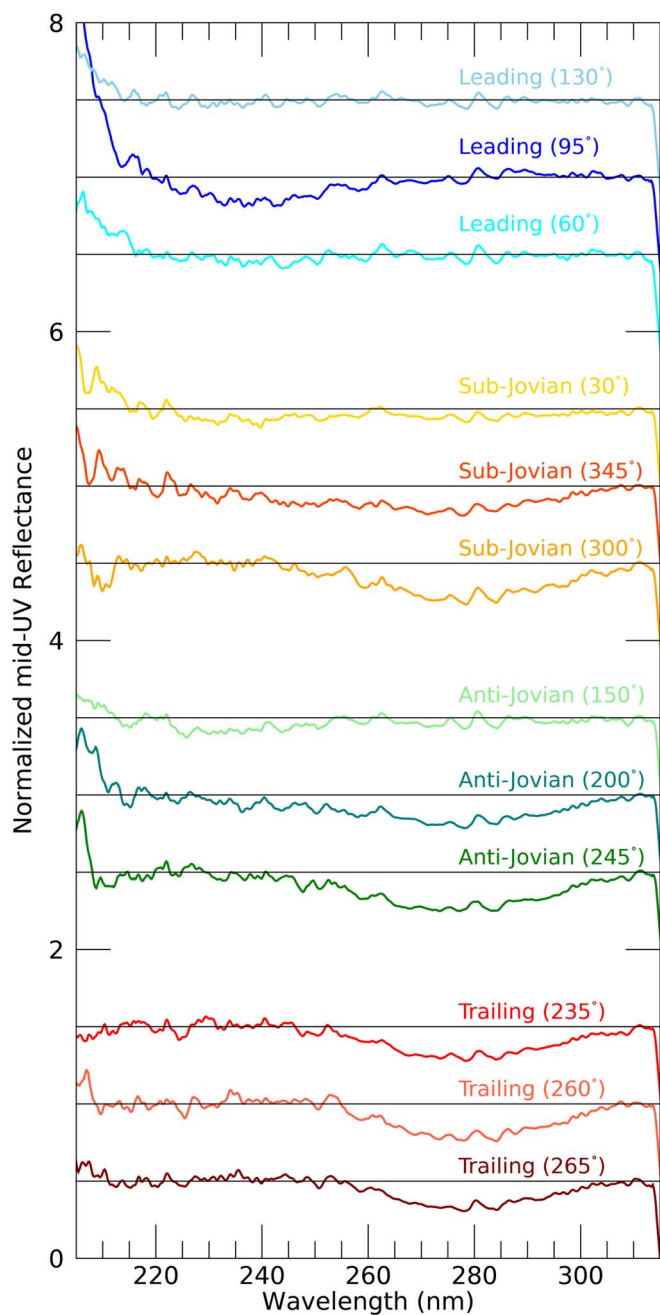
Figure 4. Normalized, continuum-removed spectra from the leading, trailing, sub-Jovian, and anti-Jovian hemispheres. We include one spectrum from pixels near the top, center, and bottom of the slit for each hemisphere; the approximate corresponding west longitude of those pixels is listed for reference. These example spectra show a clear variation in the strength of the 280 nm absorption feature in each hemisphere and the presence of the 230 nm feature on the leading hemisphere.

subtracting the minimum value of the parabolic fit from the normalized continuum signal of 1.

After determining the shape and depth of the 280 nm spectral feature of the binned pixels near the trailing hemisphere, we repeat the same calculations for each individual STIS pixel using an identical technique. All of the spectra acquired on the trailing hemisphere display the 280 nm feature. None of the spectra from the leading hemisphere display a 280 nm feature, though the 230 nm feature is identifiable in much of the leading hemisphere spectra (see Trumbo et al. 2022 for the distribution

of this feature). The 230 nm feature is broad (200–260 nm) but relatively shallow, especially compared with the 280 nm feature.

In some pixels on the anti-Jovian and sub-Jovian hemispheres, both the 280 and 230 nm features are present and overlapping (see Figure 3). This overlap appears to broaden the 280 nm feature. While we still only calculate the band area between 253.8 and 305.8 nm, we acknowledge that there is likely some overestimation of the band area that results from the contribution of the 230 nm feature. When this overlap occurs, the band center is shifted deeper into the UV. If that shift causes the band center to be shortward of 275 nm, we force the band depth calculation to occur at 279.4 nm (where it is observed near the apex of the trailing hemisphere). This prevents the band depth measurements from being affected by the 230 nm feature. If the overlap causes our fitting routine to indicate that the minimum of the parabolic fit is a wavelength shorter than 265 nm, then we assume that the 280 nm feature is completely corrupted by the 230 nm feature and cannot be assessed (or the 280 nm feature is not present at all). The linear fit used to remove the spectral continuum is impacted slightly when the 230 nm feature is present, though the feature is relatively shallow, minimizing the effect on the interpretation of the 280 nm feature.

The presence and strength of the 280 nm absorption feature vary across Europa's surface, as shown in Figure 4. The feature is most prevalent in the data acquired on the trailing hemisphere and is not present at all in the observations of the leading hemisphere. The presence of the 230 nm feature affects the continuum removal most at the shorter wavelengths, as shown most clearly for the leading hemisphere in Figure 4, where it is most abundant in the leading hemisphere chaos terrain (Trumbo et al. 2022). Trumbo et al. (2022), Brown et al. (2022), and Denman et al. (2022) attributed this feature to irradiated sodium chloride on the surface.

4. SO₂ Maps

In order to produce spatially resolved maps of our obtained SO₂ band strengths, we calculate the precise geographic coordinates of the pixel corresponding to each extracted HST spectrum. We query JPL Horizons[10] (Giorgini et al. 1996) to obtain the phase, angular size, and north pole orientation of Europa for the time of each exposure and then use the slit geometry information included in the HST FITS headers to determine the coordinates of the corners of each pixel. When mapping the pixels, we leave off those with more than one corner off the limb of Europa and average the band strengths in regions of overlap. Using this method, we obtain the SO₂ distribution shown in Figure 5.

We find that the band depths near the apex of the trailing hemisphere range between 15% and 25%. Based on the results published from the disk-integrated trailing hemisphere observations by HST FOS, Noll et al. (1995) detected a band depth of ~25%. These measurements are consistent with one another, though it is slightly surprising that the Noll et al. (1995) disk-integrated spectra, which averaged a much larger region, had a band depth equivalent to the strongest depths detected near the apex of the trailing hemisphere in the HST STIS data.

Also in agreement with past observations, the SO₂ is constrained to the sulfur-bombarded trailing hemisphere, with a
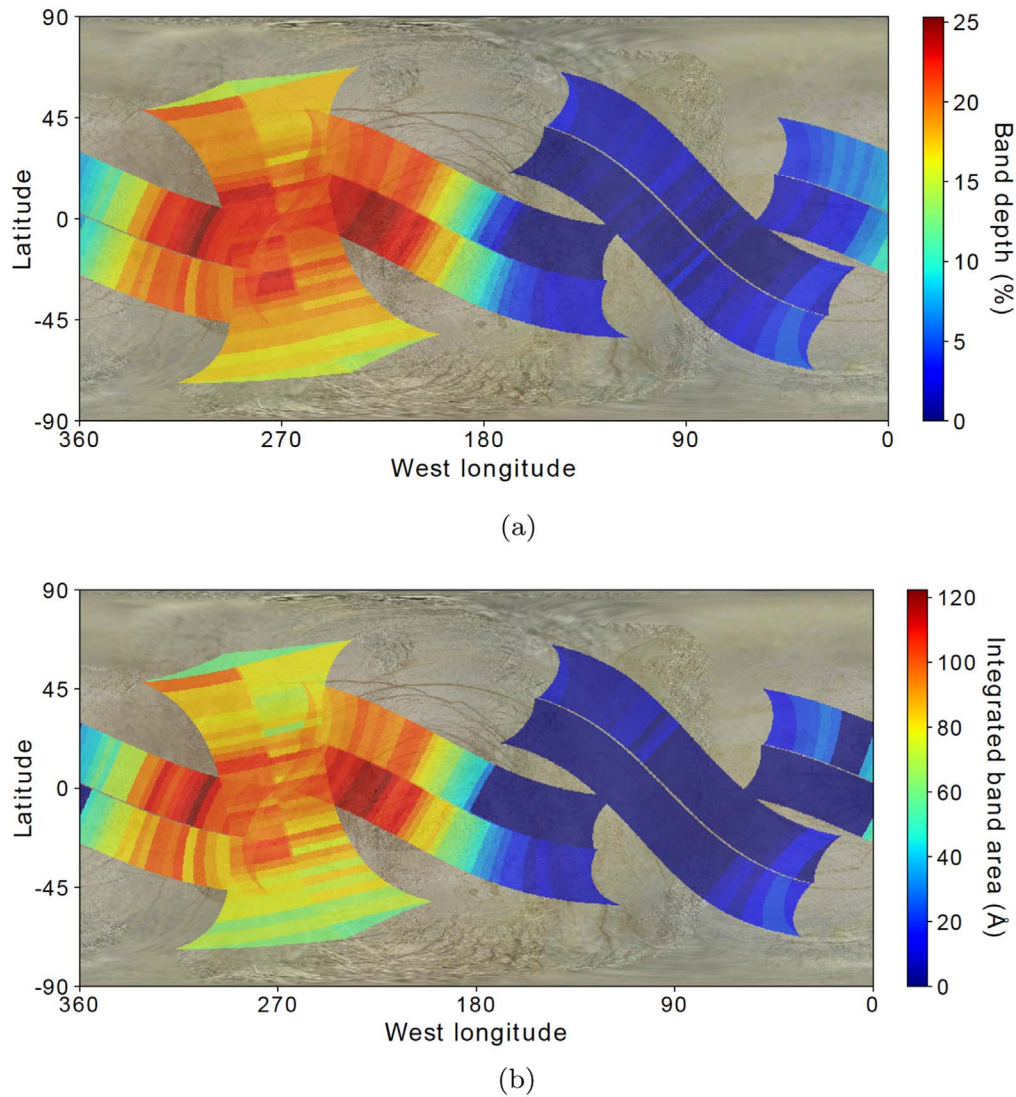
---

[10] https://ssd.jpl.nasa.gov/horizons/

(a)

(b)

Figure 5. Map of SO$_2$ (a) band depth and (b) band area for all four HST visits. We leave off pixels with more than one corner off the limb of Europa and average the band strengths in regions of overlap. These plots are two representations of essentially the same information, the strength and overall area of the absorption feature, and therefore unsurprisingly agree qualitatively. In agreement with past results, we find that the SO$_2$ is constrained to the trailing hemisphere (between ∼180°W and 360°W), with preferential concentration toward the apex (0°N, 270°W). Europa base image courtesy of NASA/JPL/Bjorn Jonsson.

preferential concentration toward the apex (0°N, 270°W). In fact, we see very sharp boundaries at almost exactly 180°W and 360°W, which strongly suggests that the SO$_2$ is largely an exogenic product produced radiolytically from Iogenic sulfur implanted onto the trailing hemisphere (Section 6.2).

However, we do note that the absorption feature appears to be slightly stronger at some longitudes within 45° of the trailing hemisphere apex; these appear to correspond with the visibly dark regions of Europa's surface, though not necessarily correlated with any identified geological regions of interest (e.g., chaos terrains). It is not clear from the modeling of ion implantation on Europa why the feature would not be strongest at the apex, though Addison et al. (2021) did show some variability in the S^{2+} and S^{3+} distribution on the trailing hemisphere depending on the ion energy and where in Jupiter's plasma sheet Europa is.

Figure 6 shows that the band area of the feature decreases approximately as a cosine away from the apex of the trailing hemisphere, which is similar to the cosine distribution expected for sulfur plasma implantation (Pospieszalska & Johnson 1989).

The spread in the band area strength is partly due to the stronger band strengths noted ±45° from the trailing apex described above and in part due to latitudinal variability of the SO$_2$ distribution that does not follow a perfect cosine dependence.

When we compare the SO$_2$ band depth with the UV reflectance, we see a similar trend. In Figure 7, we plot the reflectance at 295 nm (averaging from 290 to 300 nm) for the central 30 pixels of each observation versus the band depth. Here we note that band depth values <5% are within the noise of the fitting routine and therefore indicate a nondetection of the SO$_2$ feature. Similar to the analysis of Galileo data by Hendrix et al. (2011), the band depth is strongest where the reflectance in the UV is darkest. Hendrix et al. (2011) found a sharp increase in band depth near the young chaos regions on the trailing hemisphere, which they interpreted to indicate an additional, local source of SO$_2$ in that region. The HST data indicate a possible linear correlation between UV reflectance below 18% and the band depth, rather than a sharp difference; however, these data points are less reliable due to the
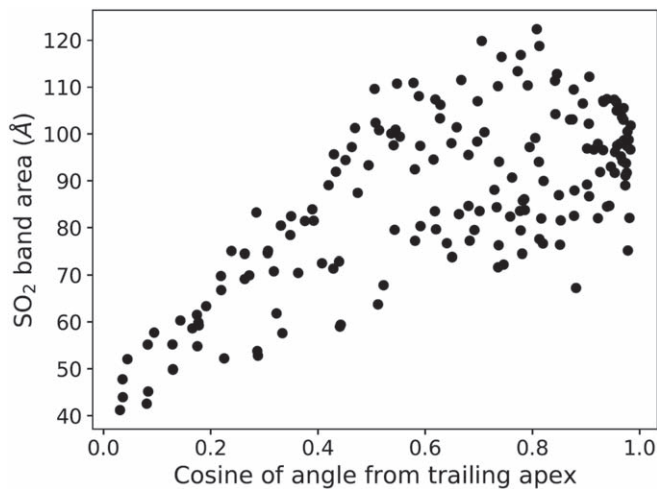
Figure 6. The SO_2 band area as a function of the cosine of the angle from the apex of the trailing hemisphere. This reveals that the band area falls roughly as a cosine away from the apex (0°N, 270°W), similar to the pattern expected for sulfur plasma implantation (Pospieszalska & Johnson 1989). The spread in band strength reflects latitudinal and longitudinal variability away from a perfect cosine dependence that may reflect factors other than sulfur implantation or could be indicative of how ion energies or Europa's position in the magnetic sheet may affect implantation and/or subsequent evolution of the species (Section 6.2).
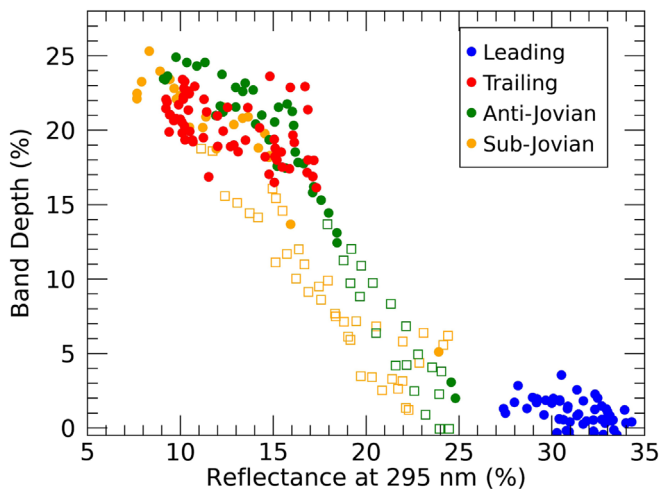

Figure 7. The SO_2 feature band depth as a function of surface reflectance averaged over 290–300 nm. Filled circles represent the most reliable measurements, while squares represent pixels that had overlapping 280 and 230 nm features and therefore produce a less reliable measurement. We note that band depths of <5% are within the noise and likely indicate a nondetection of the 280 nm feature.

overlapping 230 and 280 nm features, and the high spatial resolution of the Galileo-UVS instrument (down to 55 km pixel^{-1}) could better isolate smaller features with a higher SO_2 presence than the ~80 km pixel^{-1} along-slit, ~625 km across-slit resolution of the HST STIS observations.

5. Spectral Modeling

Previous analyses of the 280 nm absorption feature at Europa demonstrated that it is consistent with the growth of a thin film of SO_2 overlaying an H_2O substrate (Lane et al. 1981; Sack et al. 1992). This suggests that neither areal mixture models, in which SO_2 and H_2O cover distinct surface regions, nor intimate mixture models, in which discrete grains of SO_2 and H_2O are

mixed in a single region, are likely to result in an accurate representation of Europa's surface. We therefore focused on models of SO_2 trapped within H_2O grains to investigate whether this mixing method could produce the observed 280 nm feature without introducing a 4.07 μm SO_2 absorption feature, which was not detected in recent high-S/N Keck II/NIRSPEC observations (Trumbo et al. 2017) on the trailing hemisphere, though an absorption feature near 4 μm with a band depth of 5%–10% was reported in the Galileo NIMS data by Hansen & McCord (2008).

We produced intraparticle mixture models of small inclusions of SO_2 within ice grains following the method described by Molyneux et al. (2020), which uses the Maxwell Garnett rule (Garnett 1904) to produce combined optical constants of two or more materials. The reflectance of the combined material is then modeled using the Hapke bidirectional reflectance model (Hapke 1981, 1984, 1986). We used H_2O optical constants from Warren & Brandt (2008) and SO_2 optical constants from Molyneux et al. (2020; derived from absorption measurements by Mason et al. 2006) in the UV and Schmitt et al. (1994) in the IR. For the Hapke parameters B_0, h, and $\bar{\theta}$, we used values derived by Hendrix et al. (2005) and Descamps et al. (1992) from observations of Europa in the UV and IR, respectively.

Our initial UV models are shown in Figure 8. We found that inclusions of SO_2 alone produced a 280 nm absorption feature but did not match the general slope of the Europa reflectance data in the UV. We therefore added Triton tholin (McDonald et al. 1994; Cruikshank et al. 2005) to the model to modify the slope. We chose this material for the purpose of illustration because it produces a red slope in the UV and is one of the few potentially relevant materials for which both UV and IR optical constants are available in the same data set (Cruikshank et al. 2005). It is likely that other materials could produce a comparable fit to the Europa spectrum because, other than the 280 nm absorption, there are no distinct features to constrain the composition. We found that 200 μm ice grains containing 0.1% SO_2 inclusions and 0.1% Triton tholin inclusions produced a good fit to the spectral shape around 230–300 nm, although the modeled slope is slightly too steep at shorter wavelengths. This is not a unique result; we can alter the inclusion fractions to produce similar fits to the data with different H_2O grain sizes. However, the fit is sufficient to test whether it is possible to create intraparticle models that are capable of producing a 280 nm absorption feature but no (or a very weak) 4.07 μm feature.

Water ice is highly transparent around 280 nm, and the addition of a small amount of absorbing material can make a significant difference to the ice optical properties. In the 3.2–4.2 μm region, however, the ice is already very dark (Figure 9), and the addition of other materials has a much weaker effect on the reflectance model. Our model of H_2O with tholin and SO_2 inclusions was indistinguishable from pure H_2O in the IR (Figure 9(a); the intraparticle mixture is offset vertically for clarity). We also produced models including higher fractions of SO_2 (without tholin) to test how much SO_2 would be required to produce a strong 4.07 μm feature. A concentration of >20% SO_2 was needed to produce an absorption depth of >10% at 4.07 μm (Figure 9(b)). The Maxwell Garnett rule used to create the combined $H_2O + SO_2$ optical constants is only strictly appropriate for much smaller inclusion fractions, so these models are unlikely to be accurate,
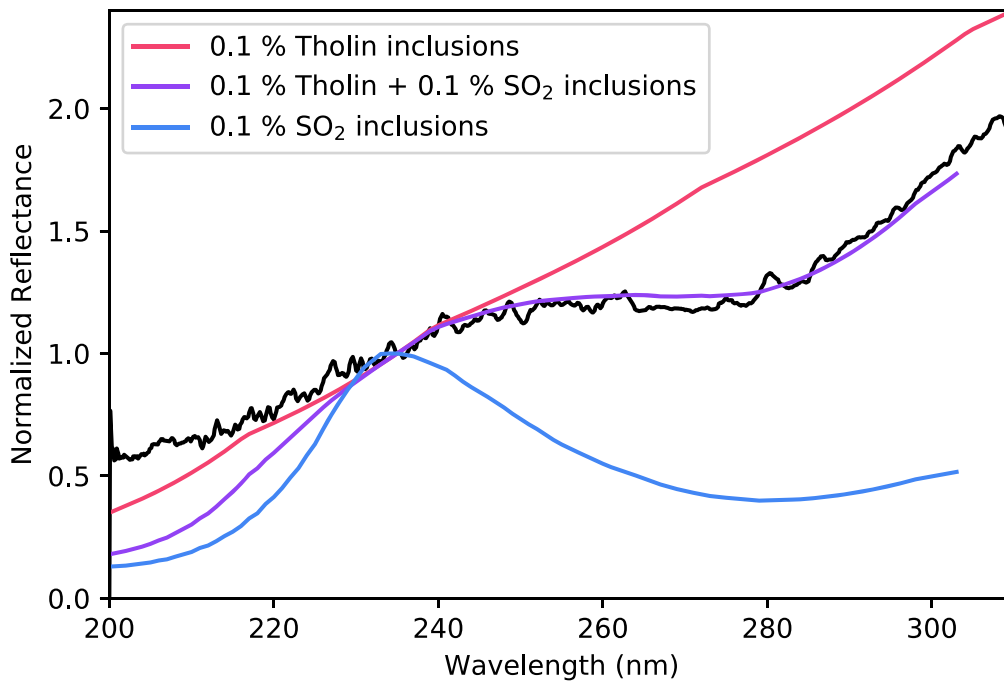
Figure 8. Intraparticle models of small inclusions within water ice. Including both a UV-absorbing tholin and the SO_2 inclusions reproduce the overall shape and strength of the 280 nm absorption feature for regions observed at the apex of Europa's trailing hemisphere.

but they indicate that no IR SO_2 feature is expected if the 280 nm absorption is produced by a small fraction of SO_2 trapped within Europa's surface ice grains.

6. Discussion

6.1. Europa's Surface Reflectance in the Mid-UV

Consistent with previous observations of Europa in the near-UV (Noll et al. 1995; Domingue & Lane 1998; Hendrix et al. 2005, 2011), the overall reflectance of Europa's surface is relatively low: <15% at 230 nm (compared to, for example, the icy satellites of Saturn; Hendrix et al. 2010; Royer & Hendrix 2014).

Europa's leading hemisphere is brighter than those of the trailing, anti-Jovian, and sub-Jovian hemispheres throughout most of the mid-UV, following a similar trend as observed at visible wavelengths. At far-UV wavelengths (100–200 nm), the differences in reflectance between hemispheres are very small, with the albedo ranging between 0.01 and 0.03 across the surface (Roth et al. 2016; Becker et al. 2018).

Of particular note, because of the gradual darkening into the shortest wavelengths, these data further confirm that Europa's surface lacks the strong, sharp water-ice spectral edge observed near 165 nm in laboratory spectra and on the icy moons and rings of Saturn (e.g., Hendrix et al. 2010; Royer & Hendrix 2014). For example, Enceladus generally displays this water-ice spectral edge feature, even though it is overall darker than pure water ice due to some absorbing agents (Hendrix et al. 2010). In the Saturnian system, ring particle collisions that "recycle" the ring material (e.g., Charnoz et al. 2009) and fresh coating of the surfaces of rings and satellites by E ring grains originating from Enceladus's plumes likely explain the persistence of such a strong water-ice feature. On Europa, however, even the relatively "pristine," water-ice-rich leading hemisphere lacks the strong far-UV signature of water, based on the observed albedo at 210 nm in this data set and that

of the far UV shown by Becker et al. (2018). This may be indicative of exposure time to surface processing including radiolysis, which may leave behind a thin, UV-absorbing lag deposit, or the presence of UV-absorbing contaminants mixed within the water ice.

Molyneux et al. (2020) showed that even small concentrations (<1%) of UV-absorbing contaminants trapped within the ice matrix can suppress the water-ice feature in the UV. They were able to reproduce the far- and mid-UV spectra of Ganymede's leading and trailing hemispheres—which also lack a 165 nm feature—using water-ice grains with inclusions of silicates, Triton-type tholins, and H_2O_2. Further analysis and modeling of the Europa HST data set will need to be conducted in order to determine the type and percentage of contaminants needed to reproduce the observations of Europa's surface, though more laboratory measurements of the optical constants of relevant materials at these wavelengths are also needed.

6.2. SO_2 Distribution on Europa

We found that the distribution of SO_2 on the surface of Europa is constrained primarily to the trailing hemisphere. The strength of the SO_2 absorption appears to be correlated with the surface reflectance between 290 and 300 nm. Unlike Hendrix et al. (2011), we do not note a sharp increase in band strength associated with geological regions; however, this could also be related to the lower spatial resolution of the HST pixels than the Galileo UV observations. Therefore, we do not rule out the possibility of some localized endogenic SO_2 in young terrains.

Multiple laboratory experiments show that hot (>10 keV) sulfur ions, which can access Europa's leading and trailing hemispheres (e.g., Cassidy et al. 2013), do not efficiently create SO_2 when irradiating pure water ice (Strazzulla et al. 2007; Dalton et al. 2013; Ding et al. 2013; Boduch et al. 2016). Cold sulfur ions (<1 keV) preferentially impinge the trailing hemisphere due to their smaller gyroradius (Cassidy et al. 2013; Addison et al. 2021). The trailing/leading asymmetry of
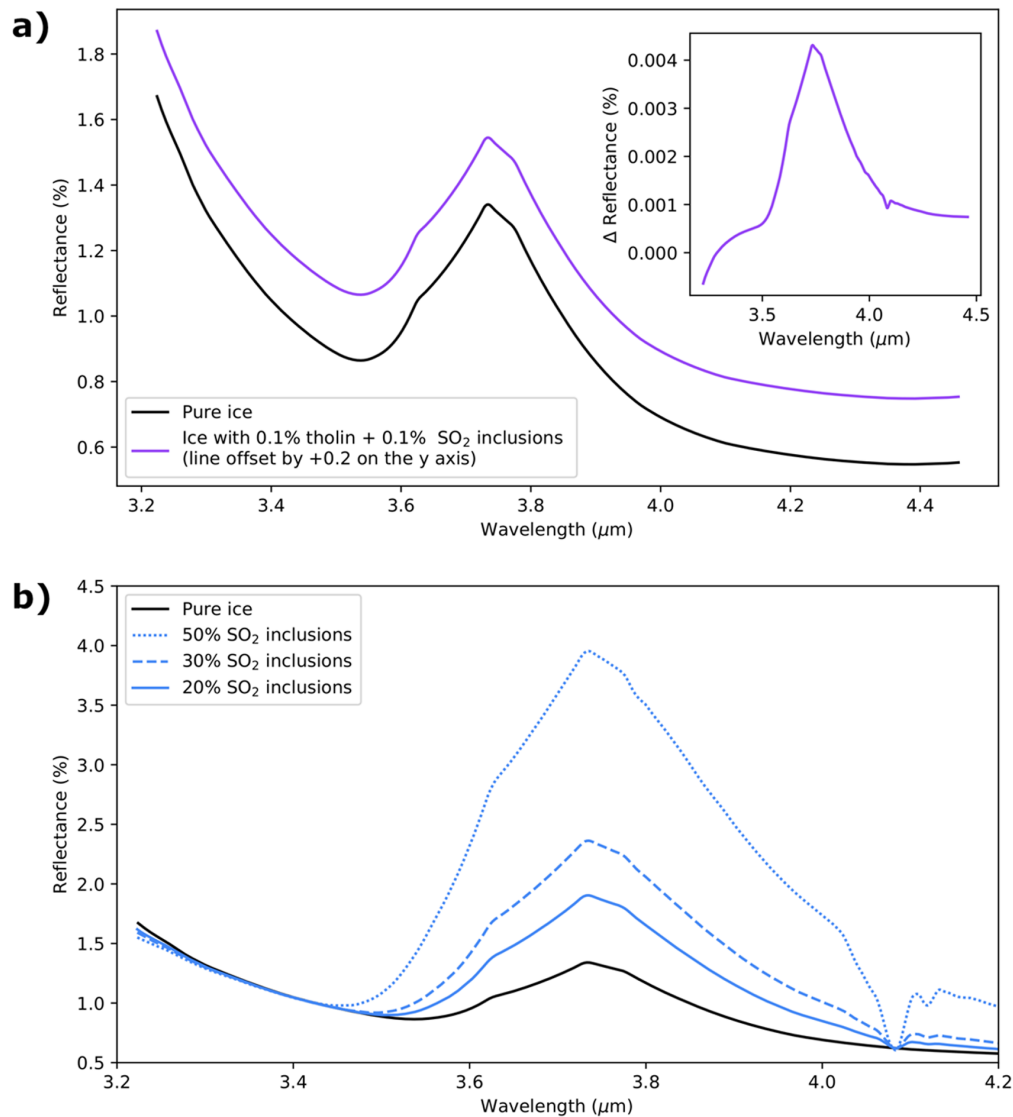
Figure 9. (Top) Comparison of the modeled IR spectrum of pure water ice and the intraparticle model parameters used to reproduce the SO_2 feature in the UV (Figure 8), offset for clarity. The inset shows the difference between the two models; the addition of the impurities changes the ice reflectance by only a few thousandths of a percentage point. (Bottom) A significant increase in SO_2 concentration is required to alter the ice optical constants enough to introduce a detectable 4.07 μm feature. Therefore, the inclusion of small concentrations of SO_2 is capable of producing the strong feature in the UV without creating a notable 4.07 μm SO_2 feature, consistent with observations of Europa's surface.

the SO_2 feature and, more importantly, the near-cosine falloff of the SO_2 band area from the trailing apex (Figure 6) are consistent with the "bullseye pattern" of the cold sulfur ion precipitation on Europa's trailing side (Pospieszalska & Johnson 1989; Hendrix et al. 2011; Cassidy et al. 2013; Addison et al. 2021). However, it is currently unclear if cold S ion radiolysis can generate SO_2 from pure water ice; laboratory experiments are needed to corroborate SO_2 synthesis in the <keV range.

While the SO_2 distribution does track with the large-scale, lower reflectances observed on Europa, SO_2 is not likely to be the only darkening agent on the surface. The leading hemisphere, which does not display the SO2 feature in the UV, is also redder than would be expected for pure water ice. This is similar to Ganymede's icy surface, which also displays a gradual increase in reflectance with wavelength across the mid-UV and lacks the water-ice spectral edge but does not have any indication of SO_2 on its surface. As discussed in

Section 6.1, Molyneux et al. (2020) instead showed that small inclusions of other materials, such as silicates, more complex species such as tholins, or H_2O_2 can reproduce the spectra observed up to 220 nm. More work is needed to understand the darkening agent in the mid-UV for both Europa and Ganymede.

Neither NASA's upcoming Europa Clipper mission nor the European Space Agency's JUICE mission will carry an instrument with a bandpass that can identify the 280 nm surface absorption feature; however, sulfur and oxygen by-products sputtered into the atmosphere may be detected at far-UV wavelengths by the Europa Ultraviolet Spectrograph (Europa-UVS) or the very similar JUICE-UVS in their designed bandpass of 55–210 nm. These Hubble observations that constrain the distribution of SO_2 across the surface may therefore assist in connecting surface–atmosphere exchange and constraining volatile transport observed by these future missions. .

7. Conclusions

Prior to this HST data set, Europa had not been observed at wavelengths between 180 and 220 nm. These observations are the first to collect high-quality, near-global, disk-resolved coverage of the UV spectrum from 210 to 315 nm.

We assess the overall mid-UV spectrum from 210 to 315 nm on the leading, trailing, anti-Jovian, and sub-Jovian hemispheres. Consistent with previous observations (e.g., Hendrix et al. 2005), we find that the spectrum is red-sloped, with the leading hemisphere becoming much brighter (by a factor of 2–3) than the other hemispheres at near-UV wavelengths ($\sim$300 nm). The low, $\sim$5% reflectance at 210 nm on all hemispheres is highly suggestive that no strong far-UV spectral edge diagnostic of water ice is present, even on the more "pristine" leading hemisphere, implying that some sort of UV-absorbing contaminant is present (Becker et al. 2018; Molyneux et al. 2020).

These spectra display two broad features: a previously unobserved feature centered near 230 nm that is primarily concentrated on the leading hemisphere, as reported by Trumbo et al. (2022), and a 280 nm feature that has been attributed to SO_2. We map the band area and depth of the 280 nm feature, which is concentrated toward the apex of the trailing hemisphere. Consistent with previous interpretations of this feature, our models show that a small concentration ($<$1%) of SO_2 trapped within water-ice grains can reproduce the strength of this feature longward of 240 nm. The large-scale distribution of the SO_2 is consistent with the emplacement of sulfur ions originating from Io preferentially emplaced on the surface by Jupiter's magnetic field.

ORCID iDs

Tracy M. Becker ⓘ https://orcid.org/0000-0002-1559-5954
Samantha K. Trumbo ⓘ https://orcid.org/0000-0002-0767-8901
Philippa M. Molyneux ⓘ https://orcid.org/0000-0002-4725-4775
Kurt D. Retherford ⓘ https://orcid.org/0000-0001-9470-150X
Amanda R. Hendrix ⓘ https://orcid.org/0000-0002-0435-8224
Lorenz Roth ⓘ https://orcid.org/0000-0003-0554-4691
Ujjwal Raut ⓘ https://orcid.org/0000-0002-6036-1575
Juan Alday ⓘ https://orcid.org/0000-0003-1459-3444
Melissa A. McGrath ⓘ https://orcid.org/0000-0003-3562-6890

References

Addison, P., Liuzzo, L., Arnold, H., & Simon, S. 2021, JGRA, 126, e29087
Becker, T. M., Retherford, K. D., Roth, L., et al. 2018, JGRE, 123, 1327
Boduch, P., Brunetto, R., Ding, J. J., et al. 2016, Icar, 277, 434
Brown, M. E., Denman, W. T. P., & Trumbo, S. K. 2022, PSJ, 3, 28
Carlson, R. W., Calvin, W. M., Dalton, J. B., et al. 2009, in Europa, ed. R. T. Pappalardo, W. B. McKinnon, & K. K. Khurana (Tucson, AZ: Univ. Arizona Press), 283
Cassidy, T. A., Paranicas, C. P., Shirley, J. H., et al. 2013, P&SS, 77, 64
Charnoz, S., Dones, L., Esposito, L. W., Estrada, P. R., & Hedman, M. M. 2009, in Saturn from Cassini-Huygens, ed. M. K. Dougherty, L. W. Esposito, & S. M. Krimigis (Dordrecht: Springer), 537
Cloutis, E. A., McCormack, K. A., Bell, J. F., III, et al. 2008, Icar, 197, 321
Cruikshank, D. P., Owen, T. C., Dalle Ore, C., et al. 2005, Icar, 175, 268
Dalton, J. B., Cassidy, T., Paranicas, C., et al. 2013, P&SS, 77, 45
Denman, W. T. P., Trumbo, S. K., & Brown, M. E. 2022, PSJ, 3, 26
Descamps, P., Arlot, J. E., Thuillot, W., et al. 1992, Icar, 100, 235
Ding, J. J., Boduch, P., Domaracka, A., et al. 2013, Icar, 226, 860
Domingue, D. L., & Lane, A. L. 1998, GeoRL, 25, 4421
Domingue, D. L., & Verbiscer, A. 1997, Icar, 128, 49
Feldman, P. D., McGrath, M. A., Strobel, D. F., et al. 2000, ApJ, 535, 1085
Garnett, J. C. M. 1904, RSPTA, 203, 385
Giorgini, J. D., Yeomans, D. K., Chamberlin, A. B., et al. 1996, BAAS, 28, 1158
Hansen, G. B., & McCord, T. B. 2008, GeoRL, 35, L01202
Hapke, B. 1981, JGR, 86, 3039
Hapke, B. 1984, Icar, 59, 41
Hapke, B. 1986, Icar, 67, 264
Hendrix, A. R., Barth, C. A., & Hord, C. W. 1998, Icar, 135, 79
Hendrix, A. R., Cassidy, T. A., Johnson, R. E., Paranicas, C., & Carlson, R. W. 2011, Icar, 212, 736
Hendrix, A. R., Domingue, D. L., & King, K. 2005, Icar, 173, 29
Hendrix, A. R., Hansen, C. J., & Holsclaw, G. M. 2010, Icar, 206, 608
Herzberg, G. 1966, Molecular Spectra and Molecular Structure, Volume 3: Electronic Spectra and Electronic Structure of Polyatomic Molecules (New York: Van Nostrand Reinhold)
Lane, A. L., Nelson, R. M., & Matson, D. L. 1981, Natur, 292, 38
Mason, N. J., Dawes, A., Holtom, P. D., et al. 2006, FaDi, 133, 311
McClintock, W. E., Rottman, G. J., & Woods, T. N. 2005, SoPh, 230, 225
McDonald, G. D., Thompson, W. R., Heinrich, M., Khare, B. N., & Sagan, C. 1994, Icar, 108, 137
Molyneux, P. M., Nichols, J. D., Becker, T. M., Raut, U., & Retherford, K. D. 2020, JGRE, 125, e06476
Noll, K. S., Weaver, H. A., & Gonnella, A. M. 1995, JGR, 100, 19057
Ockert, M. E., Nelson, R. M., Lane, A. L., & Matson, D. L. 1987, Icar, 70, 499
Pospieszalska, M. K., & Johnson, R. E. 1989, Icar, 78, 1
Roth, L., Saur, J., Retherford, K. D., et al. 2016, JGRA, 121, 2143
Royer, E. M., & Hendrix, A. R. 2014, Icar, 242, 158
Sack, N. J., Johnson, R. E., Boring, J. W., & Baragiola, R. A. 1992, Icar, 100, 534
Schmitt, B., de Bergh, C., Lellouch, E., et al. 1994, Icar, 111, 79
Spencer, J. R., Calvin, W. M., & Person, M. J. 1995, JGR, 100, 19049
Strazzulla, G., Baratta, G. A., Leto, G., & Gomis, O. 2007, Icar, 192, 623
Trumbo, S. K., Becker, T. M., Brown, M. E., et al. 2022, PSJ, 3, 27
Trumbo, S. K., Brown, M. E., Fischer, P. D., & Hand, K. P. 2017, AJ, 153, 250
Trumbo, S. K., Brown, M. E., & Hand, K. P. 2020, AJ, 160, 282
Warren, S. G., & Brandt, R. E. 2008, JGR, 113, D14220